IOP Conference Series: Materials Science and Engineering

PAPER • **OPEN ACCESS**

Measurement of heat flux in multi-layer insulated helium cryostats after loss of insulating vacuum

To cite this article: C Weber *et al* 2020 *IOP Conf. Ser.: Mater. Sci. Eng.* **755** 012155

IOP Conf. Series: Materials Science and Engineering **755** (2020) 012155 doi:10.1088/1757-899X/755/1/012155

Measurement of heat flux in multi-layer insulated helium cryostats after loss of insulating vacuum

C Weber[1,2], A Henriques[3], S Schirle[1,2] and S Grohmann[1,2]

[1] Karlsruhe Institute of Technology (KIT), Institute for Technical Physics, Hermann-von-Helmholtz-Platz 1, 76344 Eggenstein-Leopoldshafen, Germany
[2] KIT, Institute for Thermodynamics and Refrigeration, Kaiserstrasse 12, 76131 Karlsruhe, Germany
[3] European Organization for Nuclear Research (CERN), CH-1211, Geneva 23, Switzerland

E-mail: steffen.grohmann@kit.edu

Abstract. The dimensioning of pressure relief devices (PRD) for cryogenic pressure equipment requires knowledge on the heat input at the maximum credible incident. In helium cryostats, this situation is typically defined by the loss of insulating vacuum (LIV), where the heat load is induced by desublimation and condensation of atmospheric air on the cryogenic surface. This surface is often covered with multi-layer insulation (MLI) in order to reduce the thermal radiation heat load in standard operation. During loss of insulating vacuum, the MLI represents a diffusive barrier for the air to reach the cryogenic surface, reducing the heat flux as well. Experimental reference data for the heat flux in case of LIV exist mainly for blank surfaces; only few data are published for MLI-covered helium surfaces. Therefore, the effect has been investigated in the cryogenic safety test facility PICARD at KIT. This paper presents the results of venting experiments carried out with different numbers of layers and different types of MLI.

1. Introduction

Cryogenic surfaces in helium cryostats are typically covered with multi-layer insulation (MLI) in order to reduce the thermal load in standard operation. The heat flux in this case has been widely investigated for different types of MLI. A recent review is published in [1].

During the loss of insulating vacuum (LIV) that often represents the incidental scenario relevant for dimensioning of pressure relief devices (PRD) in helium cryostats, the MLI acts as diffusive barrier for the air to reach the cryogenic surface. This reduces the incidental heat flux and significantly influences the dimensioning of PRD. The measurements presented in this paper are motivated, as only few constant heat flux values are proposed in literature for this case [2]. A model in [3] developed for nitrogen dewars cannot be applied to helium cryostats, as the dominating mechanisms of desublimation and condensation on the cryogenic surface are not included.

In Section 2, we describe the experimental setup for heat flux measurements in case of LIV. The data analysis is described in Section 3 and the results are presented and discussed in Section 4. Final conclusions and an outlook are given in Section 5.

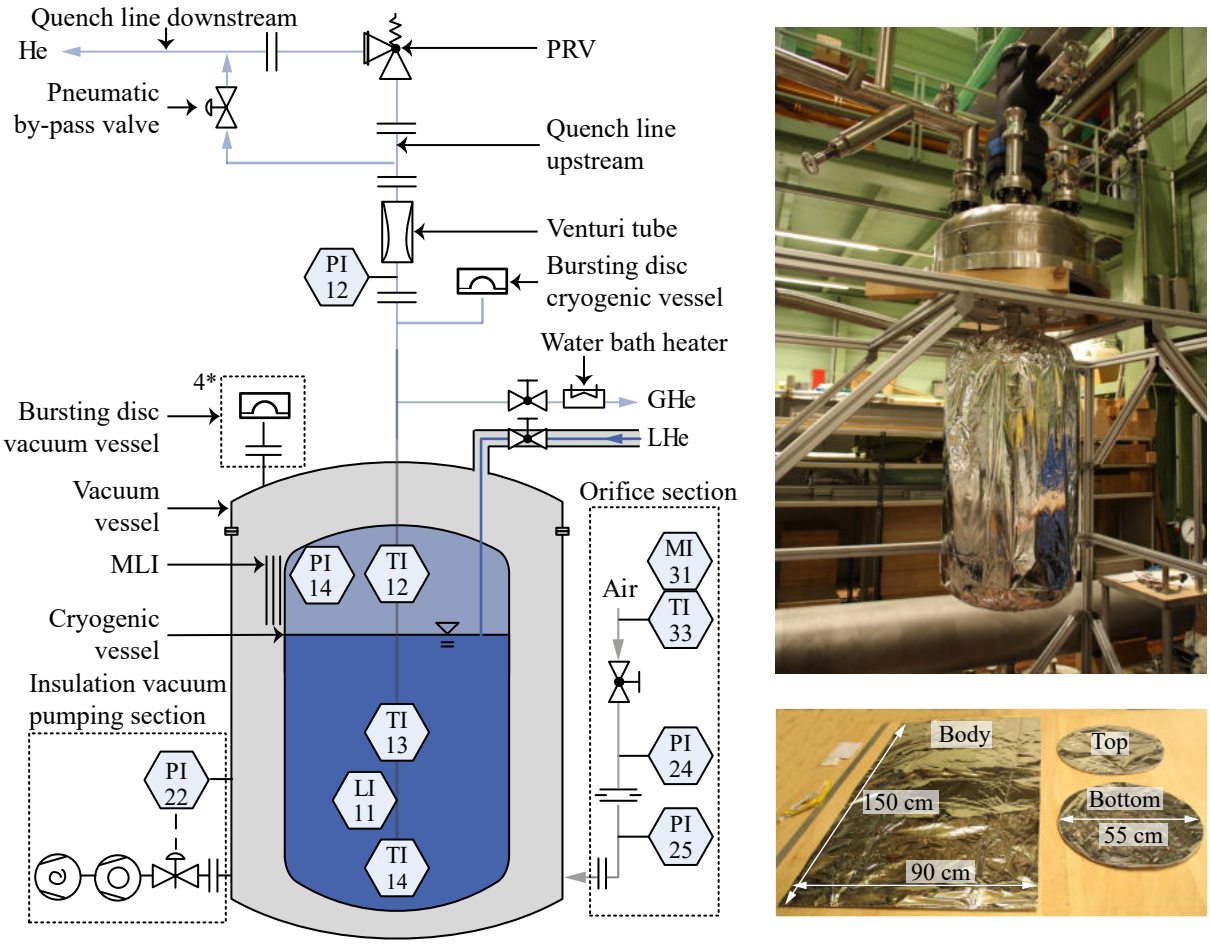

Figure 1. *Left:* Simplified P&ID chart of the PICARD test facility, updated from [4]. PI represents a pressure transmitter, PDI a differential pressure transmitter, TI a temperature sensor, LI the level sensor and MI the humidity of air. *Right:* Photograph of PICARD's cryogenic vessel wrapped with 10 layers of MLI. Dimensions of the MLI pieces used for the insulation.

2. The experimental set-up

The venting experiments are conducted at the cryogenic safety test facility PICARD. Figure 1 depicts a simplified P&ID chart of the test facility including all sensors that are relevant for the experimental evaluation of the heat flux. More detailed information on the test facility, its instrumentation and the procedure of LIV experiments are found in [4]. A pressure relief valve (PRV) with a throat diameter of 22 mm is used for all experiments presented in this paper.

Three different types of MLI are investigated:

Type 1 consists of 12 layers of 6 µm thick perforated polyester film aluminized on either side with a thickness of 40 nm and separated by polyester tulle. The films are perforated with 2 mm diameter holes in a grid of 50 mm distance. Films and tulle are assembled together.

Type 2 is a single-layer aluminium film of 6 µm thickness, bonded to a 12 µm thick aluminized polyester film, which is perforated manually with 6 mm holes in a grid of 200 mm. The matt aluminium side faces the warm surface and the glossy polyester side faces the cold surface.

Type 3 is composed of 10 layers of 12 µm thick polyester foil, double-side aluminized with a

thickness of 40 nm and interleaved with 10 layers of non-woven polyester spacer material. The perforations have a diameter of 4 mm in a grid of 150 mm.

The following precautions are taken into account for the installation on the cryogenic vessel [5]:

- the MLI is packed loosely with ≈ 10 layers/cm in order to reduce thermal conduction,
- contact between the warm outer layer and the cold inner layer is avoided,
- when blankets meet at corners, the cold layers are overlaid, tacked, folded and attached with aluminium adhesive tape,
- for straight overlaps, layers of the same temperature are stacked on top of each other,
- gaps in the MLI are avoided.

3. Data analysis

3.1. Physical properties

The experimental data is evaluated with the computer algebra system Mathematica [6]. Fluid properties of the venting fluid (air) and the cryogenic fluid (helium) are implemented as functions of temperature and pressure via REFPROP [7–12]. At wall temperatures above the triple point of pseudo-pure dry air (59.75 K), humid air is considered as a gas-steam mixture, where the gaseous phase consists of the inert dry air and the condensible water, while the liquid phase consists of water only. At $T < 59.75\,\mathrm{K}$, an ideal mixture is assumed, considering the sensible and latent heat of all humid air components with the solid enthalpies or heat capacities according to [13–15]. Material data for the cryogenic vessel are taken from Cryocomp [16].

3.2. Calculation of the wall temperature profile

Figure 2 schematically depicts the heat transfer mechanism of an MLI-insulated cryogenic vessel. The wall temperatures on the outer and the inner surface, $T_{\mathrm{W_o}}$ and $T_{\mathrm{W_i}}$, are calculated[1] by the one-dimensional transient heat transfer equations

$$\frac{\mathrm{d}T_{\mathrm{W,o}}}{\mathrm{d}t} = \frac{A_{\mathrm{Cr}}}{c_{\mathrm{Cr}} \cdot M_{\mathrm{Cr}}} \cdot \left(\dot{q}_{\mathrm{Dep}} + \dot{q}_{\mathrm{Rad}} + \dot{q}_{\mathrm{Cond}} - \dot{q}_{\lambda,\mathrm{W}}\right) \tag{1}$$

$$\frac{\mathrm{d}T_{\mathrm{W,i}}}{\mathrm{d}t} = \frac{A_{\mathrm{Cr}}}{c_{\mathrm{Cr}} \cdot M_{\mathrm{Cr}}} \cdot \left(\dot{q}_{\lambda,\mathrm{W}} - \dot{q}_{\mathrm{He}}\right) \tag{2}$$

where A_{Cr} is the outer surface of the cryogenic vessel, c_{Cr} the specific heat capacity of the vessel material at the mean temperature $T_{\mathrm{W}} = 1/2\,(T_{\mathrm{W,o}} + T_{\mathrm{W,i}})$, M_{Cr} the mass of the vessel, $\dot{q}_{\mathrm{Dep}}$ the heat flux due to humid air deposition, $\dot{q}_{\mathrm{Rad}}$ the heat flux due to thermal radiation, $\dot{q}_{\mathrm{Cond}}$ the heat flux due to thermal conduction of residual gas, $\dot{q}_{\lambda,\mathrm{W}}$ the heat flux due to thermal conduction in the vessel wall and $\dot{q}_{\mathrm{He}}$ the heat flux transferred to helium. The heat flux due to natural convection between the N^{th} MLI layer and the wall and among the MLI layers can be neglected at Grashof numbers of $\mathrm{Gr} < 2860$ [3].

3.3. Calculation of the deposition heat flux

The heat flux $\dot{q}_{\mathrm{Dep}}$ is calculated from the deposition mass flow rate $\dot{M}_{\mathrm{Dep}}$ and the enthalpy difference of humid air between ambient (Index: amb) to wall (Index: W) conditions

$$\dot{q}_{\mathrm{Dep}} = \frac{\dot{M}_{\mathrm{Dep}}}{A_{\mathrm{Cr}}} \cdot \left(h_{\mathrm{air}}\left(p_{\mathrm{amb}}, T_{\mathrm{amb}}, \varphi_{\mathrm{amb}}\right) - h_{\mathrm{air}}\left(p_{\mathrm{V}}, T_{\mathrm{W_o}}, \varphi_{\mathrm{amb}}\right)\right) \tag{3}$$

[1] The evaluation of direct wall temperature measurements in the set-up yields thermodynamically inconsistent results due to the sensor size and insufficient thermal contact and shielding, respectively.

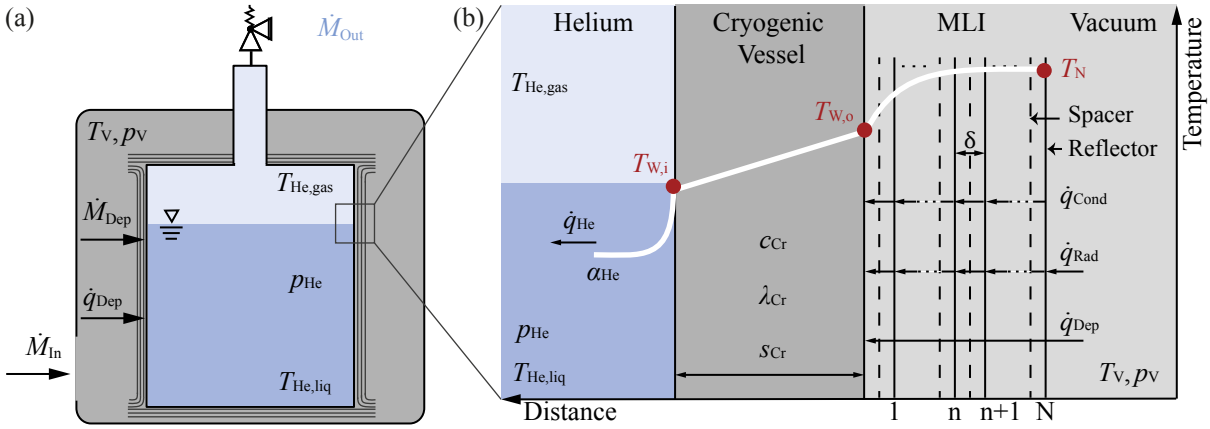

Figure 2. (a) Schematic representation of an MLI-insulated cryogenic vessel with the measuring variables relevant for the heat flux analysis; (b) zoom into the schematic temperature profile between the N^{th} MLI layer and the helium in the cryogenic vessel with the heat transfer coefficient α, the thermal conductivity λ and all relevant heat fluxes $\dot{q}$.

where p_{amb} = PI24, T_{amb} = TI33 and φ_{amb} = MI31 are the ambient air pressure, temperature and humidity, respectively while p_{V} = PI22 is the vacuum pressure. The deposition mass flow rate $\dot{M}_{\text{Dep}}$ is calculated from the ideal gas law differentiated with respect to time according to [4]. A deposition of the leaking air on MLI layers can be excluded, as their temperatures are above the condensation temperature.

3.4. Calculation of the thermal radiation heat flux

The heat flux calculation $\dot{q}_{\text{Rad}}$ is based on the Stefan-Boltzmann equation, considering N reflective MLI layers as grey emitters [17]

$$\dot{q}_{\text{Rad}} = \sigma \cdot \left(T_{\text{V}}^4 - T_{\text{W}}^4\right) \cdot \left(\left(\frac{1}{\epsilon_{\text{Cr}}} + \frac{1}{\epsilon_{\text{MLI}}} - 1\right) + (N-1) \cdot \left(\frac{2}{\epsilon_{\text{MLI}}} - 1\right) + \left(\frac{1}{\epsilon_{\text{MLI}}} + \frac{1}{\epsilon_{\text{V}}} - 1\right)\right)^{-1} \quad (4)$$

where σ is the Stefan-Boltzmann constant, $T_{\text{V}} = T_{\text{amb}}$ = TI33 is the temperature of the vacuum vessel having an emissivity $\epsilon_{\text{V}} = 0.8$ of oxidized stainless steel. For the emissivities of the cryogenic vessel and the reflective MLI layers, values of electro-polished stainless steel $\epsilon_{\text{Cr}} = 0.07$ and electro-polished aluminium $\epsilon_{\text{MLI}} = 0.04$ are assumed, respectively.

3.5. Calculation of the gas conduction heat flux

Based on the Fourier equation, the heat flux due to gas conduction between two reflective screens is calculated according to [3] as

$$\dot{q}_{\text{Cond,n}} = \frac{(r_{\text{n+1}} - r_{\text{n}}) \cdot (T_{\text{n+1}} - T_{\text{n}})}{r_{\text{n}} \cdot \left(R_{\text{g}} + \frac{R_{\text{s}} \cdot R_{\text{s}}'}{R_{\text{s}} + R_{\text{s}}'} + R_{\text{r}}\right) \cdot \ln\left(\frac{r_{\text{n+1}}}{r_{\text{n}}}\right)} \quad (5)$$

where $r_{\text{n+1}}$ and r_{n} are the radii of the $(\text{n+1})^{\text{th}}$ and n^{th} screen position, respectively. R_{g}, R_{s}, R_{s}' and R_{r} are the thermal resistance of the gaseous air, the fiber spacer, the gas inside the fiber spacer and the reflective screens. The thermal resistances R are defined as the ratio of thickness to thermal conductivity, with the values given in Table 1. The distance between two reflector layers is calculated from the packing density given in Section 2.

Table 1. MLI properties, including the thickness δ and thermal conductivity λ of both the reflector layer (R) and the spacer (S).

Type	$\frac{N_{\text{Layer}}}{\text{Blanket}}$	δ in µm		λ in $\text{Wm}^{-1}\text{K}^{-1}$	
		δ_R	δ_S	λ_R	λ_S
1	12	6	55	17	0.004
2	1	18		17	
3	10	12	55	17	0.004

Table 2. Experiments E0 to E4. The PRV has a throat diameter of 22 mm. In order to ensure safe operation, the set pressure is varied at constant throat diameter and changing heat flux.

Exp. No.	Type	N	p_set in bar(g)
E0	-	0	3.0
E1	Type 2	1	6.0
E2	Type 1	12	4.5
E3	Type 1	24	3.0
E4	Type 3	10	3.1

3.6. Calculation of the wall conduction heat flux

The heat flux due to thermal conduction in the cryogenic vessel wall $\dot{q}_{\lambda,\text{W}}$ is calculated by the Fourier equation

$$\dot{q}_{\lambda,\text{W}} = \frac{\lambda_\text{Cr}}{s_\text{Cr}} \cdot (T_{\text{W,o}} - T_{\text{W,i}}) \tag{6}$$

where λ_Cr is the thermal conductivity of stainless steel at average wall temperature T_W and s_W is the thickness of the wall.

3.7. Calculation of the heat flux transferred to helium

The convective heat flux transferred to helium is calculated by

$$\dot{q}_\text{He} = \alpha_\text{He} \cdot (T_{\text{W,i}} - T_\text{He}) \tag{7}$$

where α_He is the heat transfer coefficient to helium and T_He is the helium bulk temperature. Different correlations for α_He at sub- and supercritical states of helium are implemented. In addition to the considerations in [18], the gaseous heat transfer at sub-critical pressure is considered by a correlation for vertical cylinders according to [19]. This requires the separation of the heat transfer surface A_Cr in Equation 2 in a wetted and a dry part, using the initial filling level LI11. The liquid helium temperature is calculated as $T_\text{He,liq} = {}^1\!/_2\,(\text{TI13} + \text{TI14})$ and the gaseous temperature is $T_\text{He,gas} = \text{TI12}$. At supercritical pressure, the helium temperature is calculated as the mass-weighted average of the initial sub-critical liquid and gaseous phases. This is necessary because of stratification over the hight inside the helium as shown in Figure 3.

4. Experimental results and discussion

The experimental conditions of 4 MLI experiments are summarized in Table 2. First, the influence of different MLI configurations on the deposition heat flux $\dot{q}_\text{dep}$ is evaluated. It dominates the heat transfer into the cryogenic system and is responsible for a complex shape of the heat flux profile shown in Figure 5a). Quantifely, the total heat flux transferred to the outer cryogenic vessel surface averages to 90.9 % deposition, 9.0 % thermal conduction and 0.1 % thermal radiation.

In order to illustrate the influence of MLI on the deposition process, experiment E4 (black line) with 10 layers of MLI is compared to an experiment with a bare surface (red line). Figure 4 shows the heat flux transferred to the outer surface ($\dot{q}_\text{Dep} + \dot{q}_\text{Rad} + \dot{q}_\text{Cond}$) for both cases during

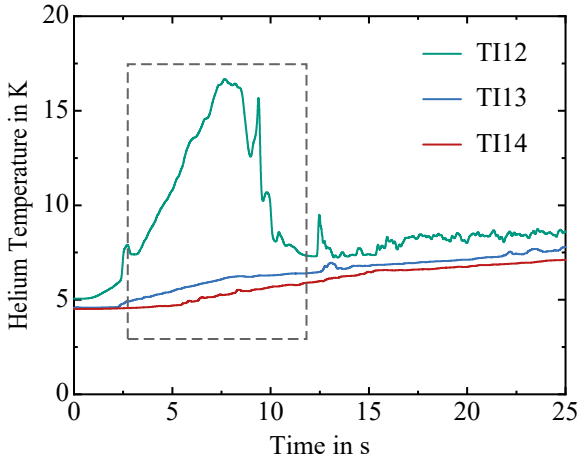

Figure 3. Helium temperature increase over time inside the cryogenic vessel for the first 25 s after the start of the venting process exemplary during experiment E4.

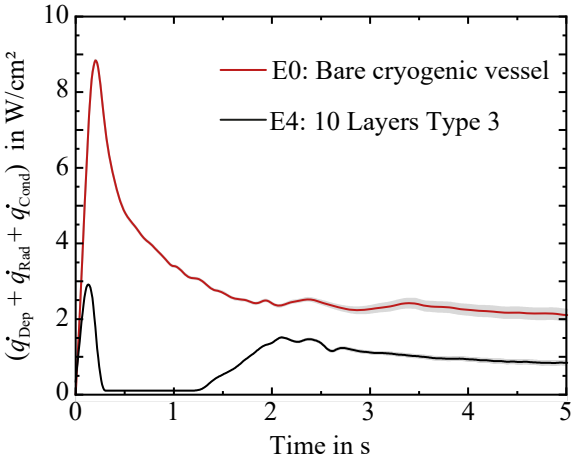

Figure 4. Zoom into the first 5 s of the heat flux transferred to the cryogenic vessel wall for experiment E0 with a bare surface and E4 calculated based on Equation 1 to 7. The measurement uncertainty according to [20] is displayed in grey.

the first 5 s after the start of venting. Similar to the bare surface, the heat flux in E4 exhibits a sharp peak within the first 0.3 s due to air molecules being able to penetrate the loosely wrapped MLI through the perforations and thus deposit on the cold surface. As the PRV is still closed, this peak is not safety-relevant. After 0.3 s, the deposition heat flux drops to almost zero, when the maximum incoming mass flow rate is reached and the MLI layers are compressed, building a diffusive barrier. The low remaining heat flux is to 99.9 % thermal convection. After 1.2 s, the incoming mass flow rate decreases, resulting in a decompression of the MLI layers. Hence, the deposition process continues and the heat flux increases again. This behaviour is observed in all configuration in Figure 5a), except for experiment E1 with the single layer (dotted line). Here, the first sharp peak is shifted in time and after 1 s, the heat flux reaches even higher values compared to the bare surface, caused by thermal conduction between the MLI layer and the wall. Experiments E2 and E3 with 12 (dashed line) and 24 layers (dotted dashed line) of MLI Type 1 show a lower impact on the reduction of the deposition heat flux than experiment E4 with 10 layers of Type 3. This is explained by the open perforation area, which in case of Type 1 is 2.3 times larger compared to Type 3.

Figure 5b) shows the heat flux profiles to helium for all investigated MLI configurations during the first 25 s after the start of the venting process. Compared to Figure 5a), the differences in heat flux cause a wall temperature increase as a function of heat capacity of the cryogenic vessel. For the dimensioning of the PRV, only the heat fluxes $\dot{q}_{He}$ at the first PRV opening are relevant, which is indicated with dots including their measurement uncertainty. The reference experiment E0 (red line) with the bare surface yields a heat flux of $(1.35 \pm 0.10)\,\mathrm{W\,cm^{-2}}$. This is reduced by 9 % to $(1.23 \pm 0.05)\,\mathrm{W\,cm^{-2}}$ in experiment E1 (dotted line) conducted with the single MLI layer. The difference can result from the process dynamics, as the overall heat flux profiles are similar apart from the time shift within the first 3 s. The set pressure during E1 is higher than the one in E0; hence the PRV opens later and the heat flux has already decreased. The installation of 12 layers of MLI Type 1 in E2 (dashed line) reduces the heat flux at the first opening more significant by 22 % to $(0.96 \pm 0.05)\,\mathrm{W\,cm^{-2}}$. In contrast to E1, a reduction of the overall heat flux profile is observed. Doubling the number of layers in E3 (dotted dashed

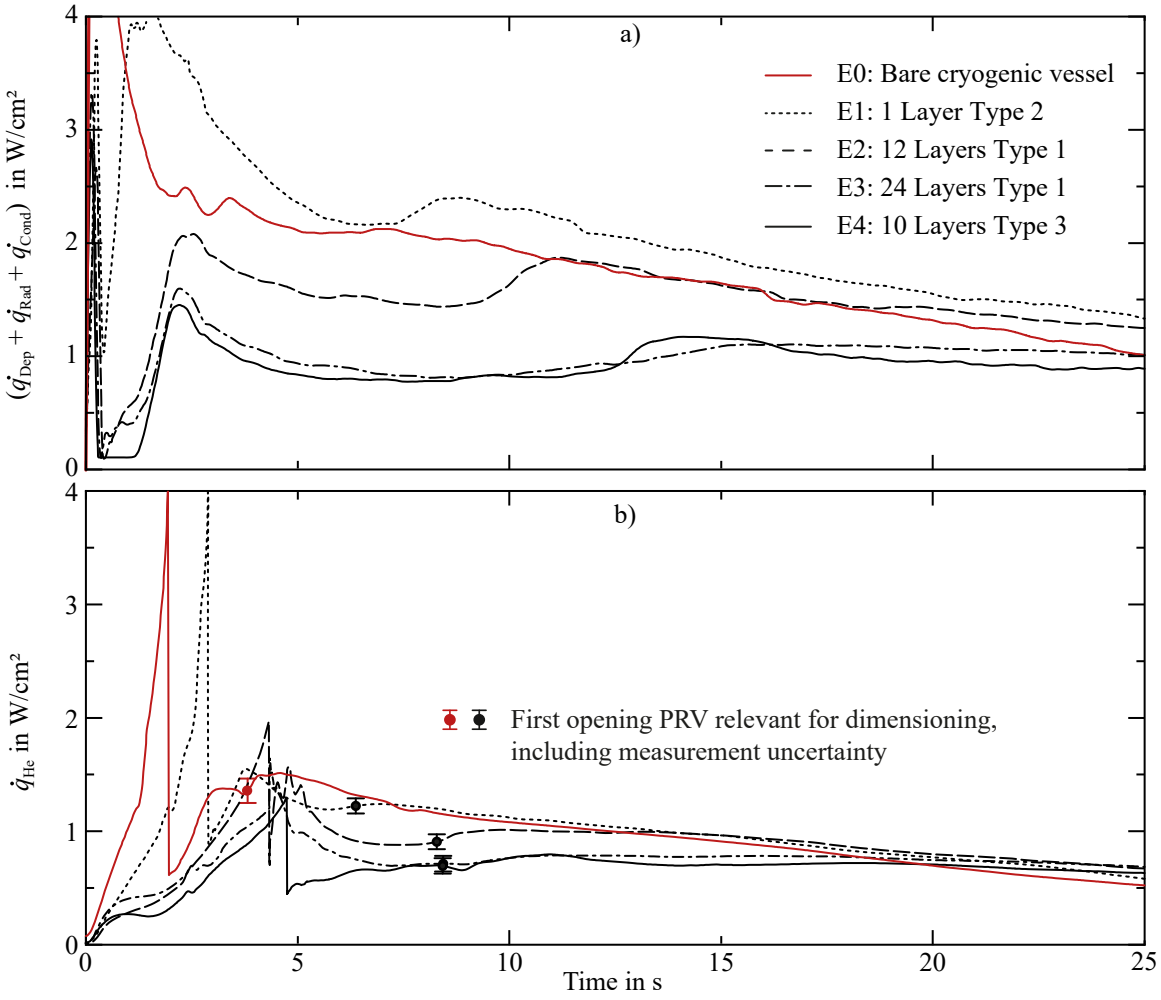

Figure 5. a) Heat flux transferred to the cryogenic vessel wall and b) heat flux transferred to helium for experiment E0 with a bare surface and experiment E1 to E4 calculated based on Equation 1 to 7. The values relevant for dimensioning at the first opening of the PRV including their measurement uncertainty bars are highlighted in b).

line) further decreases the heat flux by 26 % to $(0.71 \pm 0.07)\,\mathrm{W\,cm^{-2}}$. In experiment E4, the same result of $(0.70 \pm 0.07)\,\mathrm{W\,cm^{-2}}$ is obtained with only 10 layers of MLI Type 3 (black line). The main differences between Type 1 and Type 3 are the open perforation areas as well as the thickness of the reflective screens.

In summary, the following conclusions can be drawn from these experiments:

1. A single MLI layer does not reduce the heat flux during LIV.
2. The heat flux to helium is reduced by increasing the number of MLI layers.
3. The heat flux to helium depends on the type of MLI, influenced by the perforation area and the internal structure.

Table 3 compares the experimental results to commonly applied literature data. For a bare surface, the present experiments show significantly lower heat flux values (−63 %) at the first opening of the PRV. This applies also for the insulation with a single MLI layer, whereby its insulation effect is marginal compared to the bare surface, as explained above. In contrast, the

Table 3. Comparison of literature data from [2] with the experimental results

Cryogenic vessel insulation	Literature data [2]	Experimental results
Bare vessel	$3.8\,\mathrm{W\,cm^{-2}}$	$1.4\,\mathrm{W\,cm^{-2}}$
Single MLI layer	$2.0\,\mathrm{W\,cm^{-2}}$	$1.2\,\mathrm{W\,cm^{-2}}$
10 (12) MLI layers	$0.6\,\mathrm{W\,cm^{-2}}$	$0.7\,\mathrm{W\,cm^{-2}} \ldots 1.0\,\mathrm{W\,cm^{-2}}$

measured heat flux values for 12 layers of MLI in experiment E2 is 67 % above the value for 10 layers in [2], whereby the value in E4 is 17 % higher. This illustrates that the type of MLI is a sensitive parameter, which is not recorded in [2].

5. Conclusion and outlook

The heat flux in multi-layer (MLI) insulated helium cryostats after loss of insulating vacuum is investigated with the cryogenic safety test facility PICARD. Four experiments with three types of MLI and different layer numbers are conducted. The heat flux transferred to helium at the first opening of the pressure relief valve decreases with increasing number of layers. The MLI type, however, has a larger impact than the layer number, influenced by the perforation area and the internal MLI design. A comparison of the present work with literature yields lower values for bare surfaces and single layer insulation, while larger heat flux values are measured for MLI insulated surfaces.

The perforation of the reflective screens is identified to be a sensitive value and will be further investigated. Moreover, the influence of MLI will be implemented in a dynamic heat transfer model for the dimensioning of PRD, which already exits for bare surfaces [4, 18].

References

[1] Sutheesh P M and Chollackal A 2018 *IOP Conf. Ser. Mater. Sci. Eng.* **396** 012061
[2] Lehmann W and Zahn G 1978 *IOP Conf. Ser. Mater. Sci. Eng.* **7** 569–579
[3] Xie G F, Li, X D and Wang, R S 2010 *Cryogenics* **50**
[4] Zoller C 2018 *Experimental Investigation and Modeling of Incidents in Liquid Helium Cryostats* Ph.D. Thesis Karlsruhe Institute of Technology Karlsruhe
[5] Weisend II J G (ed) 2016 Int. Cryogenics Monograph Series (Cham: Springer)
[6] Inc W R 2018 Mathematica. Version 11.3
[7] Lemmon E W, Bell I, Huber M L and McLinden M O 2019 Refprop. Version 10.0
[8] Lemmon E W, Jacobson R T, Penoncello S G and Friend D G 2000 *J Phys Chem Ref Data* **29** 331–385
[9] Tegeler C, Span R and Wagner W 1999 *J Phys Chem Ref Data* **28** 779–850
[10] Schmidt R and Wagner W 1985 *Fluid Phase Equilib* **19** 175–200
[11] Span R, Lemmon E W, Jacobson R T, Wagner W and Yokozeki A 2000 *J Phys Chem Ref Data* **29** 1361–1433
[12] Ortiz Vega D 2013 *A new wide range equation of state for helium-4* Ph.d thesis A&M University Texas, US
[13] Iwasa Y 2009 *Case Studies in Superconducting Magnets: Design and Operational Issues* 2nd ed (Springer-Verlag US)
[14] Fagerstroem C H and Hollis Hallett A C 1969 *Journal of Low Temperature Physics* **1** 3–12
[15] Cooper J R 1982 *International Journal of Thermophysics* **3** 35–43
[16] Stewart R and Eckels 1993 – 2017 Cryocomp for windows ver. 5.3
[17] Barron R F 1999 *Cryogenic Heat Transfer* (CRC Press)
[18] Weber C, Henriques A and Grohmann S 2019 *IOP Conf. Ser. Mater. Sci. Eng.* **502** 012170
[19] Stuart W Churchill and Humbert HS Chu 1975 *Int. J. Heat Mass Transfer* **18** 1049–1053
[20] Bureau International des Poids et Mesures 2008 Evaluation of measurement data – guide to the expression of uncertainty in measurement

Acknowledgements

The authors would like to acknowledge the support from the CERN Knowledge Transfer Group and the KIT Legal Department.